

# An Improved Pattern Informatics Method for Extracting Ionospheric Disturbances Related to Seismicity Based on CSES Data: A Case Study of the Mw 7.3 Maduo Earthquake

Weixi Tian<sup>1</sup>, Yongxian Zhang<sup>2</sup>, Changhui Ju<sup>3</sup>, Shengfeng Zhang<sup>3</sup>, Maoning Feng<sup>3</sup>, and Fengli Liu<sup>4</sup>

<sup>1</sup>Institute of geophysics ,China Earthquake Administration

<sup>2</sup>Institute of Earthquake Forecasting, China Earthquake Administration

<sup>3</sup>Institute of Earthquake Forecasting,China Earthquake Administration

<sup>4</sup>Department of Earth and Space Sciences, Southern University of Science and Technology

December 27, 2023

## Abstract

The exploration of multi-layer coupling mechanisms between earthquakes and the ionosphere is crucial for utilizing ionospheric precursors in earthquake prediction. A significant research task involves continuously tracking the spatio-temporal changes in ionospheric parameters, acquiring comprehensive seismic anomaly information, and capturing “deterministic” precursor anomalies. Building upon previous research on seismic ionospheric signal characteristics and data from the China Seismo-Electromagnetic Satellite (CSES), we have enhanced the Pattern Informatics(PI) Method and proposed an Improved Pattern Informatics(IPI) Method. The IPI method enables the calculation of the spatio-temporal dynamics of electronic density anomalies detected by the CSES satellite. Taking the 2021 Maduo Mw7.3 earthquake as a case study, we analyzed the seismic signals potentially contained in the electronic density anomaly disturbances. The results show that: 1) Compared to original electronic density images, the IPI method-derived models extracted distinct electronic density anomaly signals, regardless of the data collected whether during descending (daytime) or ascending (nighttime) orbits, or across different time scales of change window. 2) The electronic density anomalies appeared about 40 days prior to the Maduo Mw7.3 earthquake. The evolution of these anomalies followed a pattern of appearance, persistence, disappearance, re-emergence, and final disappearance. Moreover, the evolution trends of the IPI hotspot images calculated from descending and ascending orbit data were similar. These results suggest that the IPI method can capture the spatio-temporal trends of ionospheric parameters and effectively extract electronic precursors related to strong earthquakes.

# An Improved Pattern Informatics Method for Extracting Ionospheric Disturbances Related to Seismicity Based on CSES Data: A Case Study of the *Mw* 7.3 Maduo Earthquake

Weixi Tian<sup>1</sup>, Yongxian Zhang<sup>2\*</sup>, Changhui Ju<sup>2</sup>, Shengfeng Zhang<sup>2</sup>, Maoning Feng<sup>2</sup>,  
Fengli Liu<sup>3</sup>

<sup>1</sup> Institute of Geophysics, China Earthquake Administration, Beijing 100081, China

<sup>2</sup> Institute of Earthquake Forecasting, China Earthquake Administration, Beijing  
100036, China

<sup>3</sup> Department of Earth and Space Sciences, Southern University of Science and  
Technology, Shenzhen 518055, China

\* Corresponding author, Email: [yxzhseis@sina.com](mailto:yxzhseis@sina.com)

## Key Points:

- Proposed an Improved Pattern Informatics Method for processing electron density data and capturing anomalous spatio-temporal pattern
- Conducted a feasibility study of the method using the 2021 Maduo *Mw*7.3 Earthquake as a case study
- Observed a recurring emergence and dissipation in the electron density prior to the Maduo *Mw*7.3 Earthquake

**Abstract:** The exploration of multi-layer coupling mechanisms between earthquakes and the ionosphere is crucial for utilizing ionospheric precursors in earthquake prediction. A significant research task involves continuously tracking the spatio-temporal changes in ionospheric parameters, acquiring comprehensive seismic anomaly information, and capturing "deterministic" precursor anomalies. Building upon previous research on seismic ionospheric signal characteristics and data from the China Seismo-Electromagnetic Satellite (CSES), we have enhanced the Pattern Informatics(PI) Method and proposed an Improved Pattern Informatics(IPI) Method. The IPI method enables the

34 calculation of the spatio-temporal dynamics of electronic density anomalies  
35 detected by the CSES satellite. Taking the 2021 Maduo *Mw*7.3 earthquake as a  
36 case study, we analyzed the seismic signals potentially contained in the electronic  
37 density anomaly disturbances. The results show that: 1) Compared to original  
38 electronic density images, the IPI method-derived models extracted distinct  
39 electronic density anomaly signals, regardless of the data collected whether  
40 during descending (daytime) or ascending (nighttime) orbits, or across different  
41 time scales of change window. 2) The electronic density anomalies appeared  
42 about 40 days prior to the Maduo *Mw*7.3 earthquake. The evolution of these  
43 anomalies followed a pattern of appearance, persistence, disappearance,  
44 re-emergence, and final disappearance. Moreover, the evolution trends of the IPI  
45 hotspot images calculated from descending and ascending orbit data were similar.  
46 These results suggest that the IPI method can capture the spatio-temporal trends  
47 of ionospheric parameters and effectively extract electronic precursors related to  
48 strong earthquakes.

49

50 **Keywords** : Improved Pattern Informatics Method(IPI Method) ; China  
51 Seismo-Electromagnetic Satellite(CSES); Seismo-Ionospheric Disturbances; *Mw* 7.3  
52 Maduo Earthquake; Earthquake Prediction.

## 53 **1. Introduction**

54 Since Gokhberg(1982) first detected pre-seismic electromagnetic signal  
55 anomalies in satellite data, several countries have incorporated electromagnetic  
56 satellite monitoring into their space development programs. These include Russia's  
57 Predvestnik-E, COMPASS-I, and II satellites, the United States' QUAKESAT, and  
58 France's DEMETER satellite. Electromagnetic satellite monitoring offers advantages  
59 over terrestrial geophysical monitoring methods due to its global reach, short periods,  
60 high efficiency, dynamism, and all-weather capabilities (Zhuo Xianjun *et al.*, 2005).  
61 The potential applications of this technology in earthquake mechanism research and  
62 seismic monitoring and prediction have made the study of pre-seismic  
63 electromagnetic anomalies using satellite data a new research hotspot (Zhang *et al.*,  
64 2023). Following the launch of the China Seismo-Electromagnetic Satellite (CSES)

65 on February 2, 2018, a series of studies have been conducted in various areas. These  
66 include data availability (Yan *et al.*, 2020; Liu *et al.*, 2021), global geomagnetic  
67 models (Yang *et al.*, 2021), ionospheric events such as magnetic storms (Spogli *et al.*,  
68 2021), statistical characteristics of seismic ionospheric disturbances (Li *et al.*, 2020;  
69 De Santis *et al.*, 2021), and multi-layer coupling (Marchetti *et al.*, 2019; Zhao *et al.*,  
70 2021; Liu *et al.*, 2023; Zhang *et al.*, 2023).

71 During the operational period of the CSES satellite, more than 500 earthquakes  
72 of magnitude 6 and above, and nearly 60 of magnitude 7 and above, occurred globally  
73 (Shen *et al.*, 2023). This provided a rich data source for studying the correlation  
74 between ionospheric observations and earthquakes. Many scholars have attempted to  
75 extract ionospheric disturbances and precursory information related to earthquakes  
76 from the vast amount of CSES satellite data (Marchetti *et al.*, 2019; Li *et al.*, 2020;  
77 Yang *et al.*, 2021; De Santis *et al.*, 2021). Statistical studies have shown a clear  
78 spatio-temporal correlation between earthquakes and electron density anomalies (Li *et al.*,  
79 *et al.*, 2020, 2023; De Santis *et al.*, 2019; Liu *et al.*, 2022). Although current research  
80 has gained an initial understanding of the spatio-temporal characteristics of seismic  
81 ionospheric precursor information, previous anomaly extraction methods, such as  
82 sliding principal component analysis (PCA) method (Chang *et al.*, 2017), Wavelet and  
83 Bispectral techniques (Sondhiya *et al.*, 2014), and quartile methods (Zhang *et al.*,  
84 2020), mostly use data from single or partial orbits, making it challenging to  
85 simultaneously capture anomalies in the epicenter and surrounding areas (Zheng *et al.*,  
86 2023). Moreover, the lower spatial resolution and discontinuous measurements of  
87 satellite observations hinder the continuous tracking of seismic-ionospheric signal  
88 changes, impacting our understanding of the temporal and spatial evolution of these  
89 signals (Zhang *et al.*, 2023). Therefore, to capture ionospheric anomalies reflecting  
90 the seismic incubation process, detect precursory anomalies related to earthquakes,  
91 and explore the multi-layer coupling mechanism between earthquakes and the  
92 ionosphere, further development and research into methods for extracting ionospheric  
93 disturbance anomalies are still needed.

94 Rundle *et al.* (2000, 2002) developed the PI method for studying earthquake  
95 activity, which has shown promising predictive performance in medium-long-term

96 earthquake forecasting. Wu et al. (2011) made modifications to the PI algorithm,  
97 proposing the Modified Pattern Informatics (MPI) method, which was successfully  
98 applied to the analysis of DEMETER satellite data anomalies, providing images of the  
99 ionospheric anomaly evolution before the Wenchuan earthquake and confirming the  
100 feasibility of applying the MPI method to electromagnetic satellite observation data  
101 processing. The MPI method, through grid-based and interpolation data processing  
102 techniques, overcomes the discontinuity and low spatial resolution issues of satellite  
103 observations. However, it has not yet considered specific data characteristics such as  
104 the orbital altitude of CSES (Liu *et al.*, 2021), nor propagation features of  
105 seismic-ionospheric signals including the range of earthquake anomaly (De Santis *et*  
106 *al.*, 2019) and negative ionospheric anomalies associated with earthquakes  
107 (Akhoondzadeh *et al.*, 2010).

108 In this study, we take into account the electron density data characteristics of the  
109 CSES satellite and the features of seismic-ionospheric signals to enhance the PI  
110 method, introducing an Improved Pattern Informatics (IPI) method. We evaluate the  
111 efficacy and reliability of this method by examining the case of the 2021 *Mw*7.3  
112 Maduo earthquake in Qinghai. Through the analysis of continuous spatio-temporal  
113 evolution images of the IPI hotspots, we identify potential ionospheric anomaly  
114 signals that emerged before and after the earthquake.

## 115 **2.Data**

### 116 2.1. Ionospheric Data Recorded by CSES

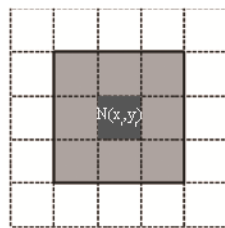
117 The China Seismo-Electromagnetic Satellite (CSES), also known as  
118 Zhangheng-1 Electromagnetic Satellite (ZH-01), is the first microsatellite for  
119 monitoring seismic electromagnetic activities (Shen *et al.*, 2018). It operates in a  
120 circular sun-synchronous orbit at an altitude of 507 kilometers, with its descending  
121 node aligning with 14:00 local time (LT) and a revisit period of 5 days. The satellite's  
122 operational region spans the latitude range of  $[-65^{\circ}, 65^{\circ}]$ . Equipped with eight  
123 payloads, including a Langmuir probe that primarily measures electron temperature  
124 and density with a one-second temporal resolution (Liu *et al.*, 2019), this study  
125 employs electron density data captured by the CSES Langmuir probe from January 1,  
126 2019, to December 31, 2021.

127 2.2. Data Process

128 The IPI method's enhanced spatio-temporal integration capability is derived from  
129 the spatial and temporal grid division of the data. Therefore, preprocessing of the  
130 CSES data is necessary to create an "Ionospheric Parameter Catalog" containing time,  
131 longitude, latitude, and observational values. The specific steps are as follows:

132 Grid Division: Based on the grid correlation of ionospheric parameters (Yao *et al.*,  
133 2014) and the orbital characteristics of the CSES satellite, the operational range of  
134 the CSES orbit is divided into grids of  $5^\circ \times 2^\circ$  (longitude  $\times$  latitude).

135 Moore Neighbor Interpolation: After grid division, it's essential to calculate the  
136 mean value of ionospheric parameters for each grid and assign it to the grid's center  
137 point. To obtain the daily two-dimensional distribution of ionospheric parameters in  
138 the CSES monitoring area and mitigate the issue of large gaps between adjacent orbits  
139 and sparse data in the longitude direction, grids without data utilize the Moore  
140 Neighboring principle (Chen *et al.*, 2005). This involves averaging the parameters  
141 from the eight neighboring grids surrounding the  $N(x_i, y_j)$  grid and assigning this  
142 average to the  $N(x_i, y_j)$  grid as the ionospheric parameter for that day, as illustrated  
143 in Figure 1.



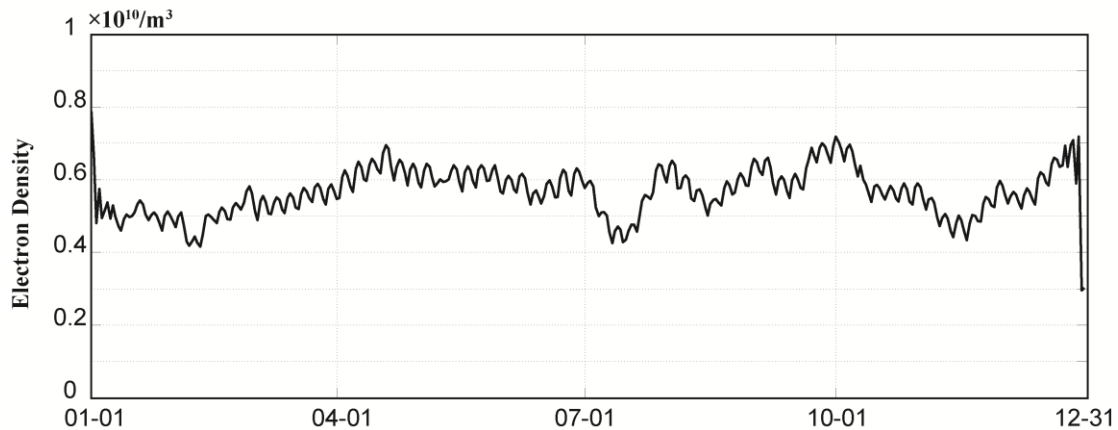
144 **Moore neighborhood**

145 Figure 1 Moore neighbor interpolation

146 Establishing an Annual Model of Ionospheric Parameters: Due to issues such as  
147 instrument malfunctions, some grids still have discontinuous data sequences.  
148 Therefore, we construct a time series for the ionospheric parameters of each grid.  
149 Using cubic spline interpolation, we interpolate these time series to create an annual  
150 model for the ionospheric parameters of all grid points.

151 Developing a Dynamic Ionospheric Background Field: Considering the annual  
152 and seasonal variations, long-term trends of the ionosphere, and factors like the  
153 Equatorial Ionization Anomaly (EIA), Weddell Sea Anomaly (WSA), and other

154 large-scale ionospheric structures (Li *et al.*, 2023), we establish a daily dynamic  
155 background field for the ionosphere, as illustrated in Figure 2. The original  
156 observational data and the residual values from the background field are used as input  
157 for the IPI method. After removing the dynamic background field of the ionospheric  
158 parameters, we obtain an "Ionospheric Parameter Catalog" containing date, latitude,  
159 longitude, and residual values.



160

161

162

Figure 2 Dynamic background field  
The grid (97.5°E, 30°N) is used as an example.

163

### 3. Method

164

#### 3.1. Pattern Informatics Method

165

166

167

168

169

170

171

172

173

PI divides a region into N grids and defines an N-dimensional system state vector built on Hilbert space (consisting of a time series of seismic times from the N grids). It considers this system state vector to represent the seismicity of a region and its value to be a constant. The phase angle of this system vector varies with time. If the relative rate of seismic activity intensity of a unit vector varies too much, its phase angle will undergo a continuous rotation away from the quantifiable average value, which is known as the drift of the phase angle. According to PI, the change in the activity pattern of small earthquakes is represented by the drift of the phase angle (Rundle *et al.*, 2000, 2002).

174

175

176

177

The process entailed dividing the study area into spatial and temporal grids, constructing a frequency time series of the seismic events larger than a certain magnitude threshold in each grid, normalizing the intensity of seismic events, calculating the deviation of the intensity function from the background in each grid

178 and calculating the probability of seismic events. The probability of seismic events in  
179 each grid was then normalized to the probability of occurrence and the grid with a  
180 high probability of seismic events was detected after deducting the background  
181 probability, i.e., "seismic hotspots"(Chen *et al.*, 2005).

### 182 3.2. Improved Pattern Informatics Method (IPI)

183 We refined the PI method to develop the IPI method, based on the characteristics  
184 of seismic-ionospheric signals and the features of CSES data. Key improvements  
185 include defining the study area, modifying the method for calculating anomalies,  
186 eliminating the spatial application of Moore's principle and the forecasting period, and  
187 computing negative ionospheric anomalies. The specific process of the IPI method is  
188 as follows:

189 (1) The study area is determined using the empirical formula for the seismogenic zone  
190 range (Dobrovolsky *et al.*, 1979), as shown in Equation (2.1) .

$$R = 10^{0.43M}$$

$$191 \quad R_{OPI} = \sqrt{2}R \quad (2.1)$$

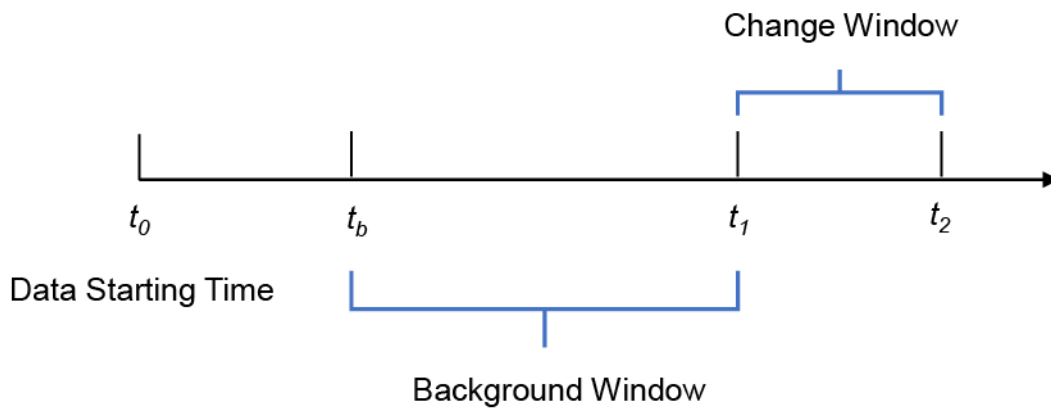
192 Where M is the magnitude, and R is the radius of the seismogenic zone.  
193 Considering the data preprocessing process where data is divided into rectangular  
194 grids, and to ensure that the study area is within the Dobrovolsky seismogenic  
195 zone range, we set the Dobrovolsky seismogenic zone as the circumscribed circle  
196 of the study area, with  $R_{OPI}$  being the side length of the square. For instance, for  
197 a  $M7.0$  earthquake, the radius  $R$  of the seismogenic zone is approximately 1023  
198 km, and the side length of the study area's square is about 1447 km.

199 (2) Grid Division: The IPI method allows for the selection of different grid sizes  
200 based on the spatial resolution of the data. However, the preprocessing, based on  
201 the findings of Yao *et al.* (2014) and the orbital characteristics of the CSES  
202 satellite, results in an "Ionospheric Parameter Catalog" with a precision of  $5^\circ \times 2^\circ$ .  
203 Consequently, the grid division for the IPI study area also adopts this size of  
204  $5^\circ \times 2^\circ$ .

205 (3) Setting a Lower Threshold  $N_c$ , and identifying anomalies using a Boolean  
206 function(Tiampo *et al.*, 2002): Each grid constructs a time series  $N_i(t)$ ,

207 representing the number of times the residual value in a given grid exceeds the  
 208 lower threshold  $N_C$  within a unit of time. In constructing  $N_i(t)$ , the spatial  
 209 Moore's principle is omitted. This is because, in seismological PI methods,  
 210 Moore's principle is applied to account for earthquake location errors, which is not  
 211 applicable to ionospheric data. The use of a Boolean function and the lower  
 212 threshold  $N_C$  categorizes values above  $N_C$  as 1 and below  $N_C$  as 0, assigning  
 213 equal weight to anomalies of varying magnitudes. This approach, in contrast to  
 214 differential calculations of absolute anomaly values (Wu *et al.*, 2011), mitigates  
 215 the impact of extreme value anomalies on the results, enhancing the stability of  
 216 anomaly detection.

217 (4) Defining Five Time Points and Two Time Windows: The time points are  
 218 designated as  $t_0$ ,  $t_b$ ,  $t_1$ ,  $t_2$ , and an arbitrary time  $t$ , illustrated in Figure 3. We have  
 219 omitted the predictive period  $t_2 \sim t_3$  (Rundle *et al.*, 2000, 2002) from our analysis.  
 220 This is based on the fact that the original PI algorithm's predictive period is  
 221 founded on the average field properties of dynamic diffusion, and whether  
 222 ionospheric parameter variations conform to this property requires further  
 223 investigation.



224

Figure 3 Time window division

225

226

$t_0$  is the start time of the data, the background time window is from  $t_b$  to  $t_1$  ( $t_0 \leq t_b \leq t_1$ ), and the change  
 227 window is from  $t_1$  to  $t_2$ .

228

Considering that a longer background window can contain more information, but  
 229 the variation of ionospheric parameters is rapid, an excessively long background  
 230 window might include irrelevant information in the calculation. Therefore, this  
 231 study selected a background window of 6 months. The selection of the change

232 window will be thoroughly described in Section 4.

233 (5) Define the ionospheric parameter intensity function as  $I_i(t_b, t)$ , and calculate the  
234 average number of instances where the grid  $i$  exceeds the minimum ionospheric  
235 parameter threshold  $N_C$  from  $t_b$  to  $t$ .

$$236 \quad I_i(t_b, t) = \frac{1}{t-t_b} \sum_{t'=t_b}^t N_i(t') \quad (2.2)$$

237 (6) By calculating the difference between the ionospheric parameter during the  
238 change window and the background window, we obtain the ionospheric parameter  
239 anomaly intensity function  $\Delta I_i(t_b, t_1, t_2)$ .

$$240 \quad \Delta I_i(t_b, t_1, t_2) = I_i(t_b, t_2) - I_i(t_b, t_1) \quad (2.3)$$

241 (7) In order to obtain the relative ionospheric parameter anomaly intensity function  
242 for each grid in the research area, normalize the ionospheric parameter anomaly  
243 intensity function.

$$244 \quad \Delta \widehat{I}_i(t_b, t_1, t_2) = \frac{\Delta I_i(t_b, t_1, t_2) - \langle \Delta I_i(t_b, t_1, t_2) \rangle}{\sigma(t_b, t_1, t_2)} \quad (2.4)$$

245 Where  $\langle \Delta I_i(t_b, t_1, t_2) \rangle$  is the average ionospheric parameter anomaly intensity  
246 function for all grids, and  $\sigma(t_b, t_1, t_2)$  is the standard deviation of the ionospheric  
247 parameter anomaly intensity function for all grids.

248 (8) To eliminate the "noise" associated with extremely small change, we calculate the  
249 average change of the normalized background anomaly ionospheric parameter  
250 according to equation (2.4).

$$251 \quad \overline{\Delta \widehat{I}_i(t_b, t_1, t_2)} = \frac{1}{t_1-t_0} \sum_{t_b=t_0}^{t_1} \Delta \widehat{I}_i(t_b, t_1, t_2) \quad (2.5)$$

252 (9) Define the probability of an anomalous disturbance occurring in grid  $i$  as  $P_i(t_0, t_1,$   
253  $t_2)$ , which is the exponential function of the absolute average change of the  
254 normalized ionospheric parameter anomaly intensity function.

$$255 \quad P_i(t_0, t_1, t_2) = e^{|\Delta \widehat{I}_i(t_0, t_1, t_2)|} \quad (2.6)$$

256 (10) The original PI did not take into account the negative ionospheric anomalies  
257 associated with earthquakes (Akhoondzadeh *et al.*, 2010; Liu *et al.*, 2022).  
258 Therefore, we have modified the formula from  $P_i(t_0, t_1, t_2) = e^{\Delta I_i(t_0, t_1, t_2)}$  (Wu

259 *et al.*, 2011) to  $P_i(t_0, t_1, t_2) = e^{|\Delta I_i(t_0, t_1, t_2)|}$ , ensuring the IPI calculation can  
260 capture both positive and negative ionospheric anomalies.

261 (11) We calculate the average probability of anomalous disturbances occurring in all  
262 grids in the research area as the background probability. The relative change is  
263 then obtained by subtracting the background probability from the individual grid  
264 probabilities.

$$265 \quad \Delta P_i(t_0, t_1, t_2) = P_i(t_0, t_1, t_2) - \langle P_i(t_0, t_1, t_2) \rangle \quad (2.7)$$

266 For grids with positive values, i.e., grids where  $P_i(t_0, t_1, t_2) > 0$ , we designate  
267 them as hotspots (anomalous areas).

268 (12) To better analyze the evolution process of seismic ionospheric signals and  
269 highlight anomalies, we can slide  $t_0$ ,  $t_1$ ,  $t_2$ , and  $t_3$  with a fixed sliding step size to  
270 obtain continuous results over multiple days. Finally, we can normalize all the  
271 results to obtain the Standard IPI hotspots (SIPI).

$$272 \quad S_{IPI} = \frac{\Delta P_i(t_0, t_1, t_2)}{\Delta P_i(t_0, t_1, t_2)_{max}} \quad (2.8)$$

## 273 **4. IPI method in the identification of spatio-temporal**

### 274 **ionospheric anomalies before the Maduo Mw7.3 earthquake**

275 On May 22, 2021, a Mw7.3 earthquake occurred in Maduo County, Qinghai  
276 Province, China (34.598°N, 98.251°E), with a focal depth of 10km. Based on the IPI  
277 method and using electron density data observed by the CSES satellite, we  
278 constructed multiple models to calculate the pre- and post-earthquake electron density  
279 anomalies in Maduo. Additionally, we analyzed the spatiotemporal dynamics of  
280 electron density using IPI hotspot maps.

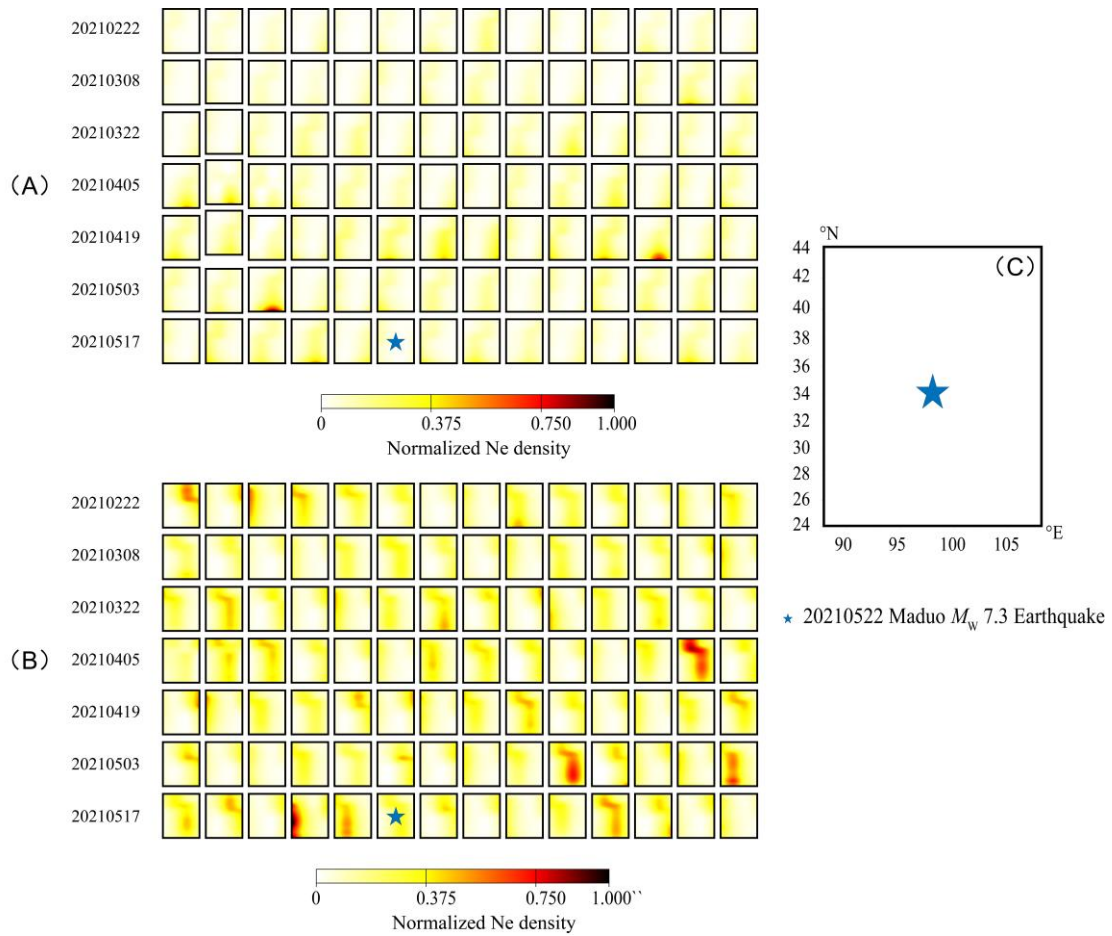
281 Due to the significant increase in ionospheric electron density caused by solar  
282 radiation during the day, nighttime data is generally used for extracting ionospheric  
283 anomalies (Guo *et al.*, 2022; Wen *et al.*, 2022). The IPI algorithm is adaptive, capable  
284 of effectively eliminating background trends and noise, and theoretically can mitigate  
285 the influence of daytime solar activities. Therefore, we processed both ascending and  
286 descending orbit data separately, computing their respective original electron density

287 images and IPI hotspot maps. This approach allowed a more comprehensive study of  
288 the spatiotemporal characteristics of electron density before the earthquake and  
289 explored the potential of this method for extracting anomalies from daytime  
290 ionospheric data.

#### 291 4.1. Spatio-temporal images with electron density

292 To dynamically track the detailed characteristics of the original electron density  
293 evolution over time, ensuring data readability and consistent measurement properties,  
294 we obtained normalized spatio-temporal images of electron density for 90 days before  
295 and 7 days after the Maduo  $M_w7.3$  earthquake, as shown in Figure 4. The study area  
296 was determined based on formula (2.3), with an  $R_{OPI}$  of approximately 1000Km.  
297 The spatial extent of the study area is marked in Figure 4, which is consistent with the  
298 subsequent IPI study region.

299 Figure 4 (A) and (B) represent the results from descending (daytime) and  
300 ascending (nighttime) data, respectively. The results indicate no significant abnormal  
301 disturbances in the original electron density observations before and after the Maduo  
302  $M_w7.3$  earthquake, rendering it impossible to derive meaningful seismic ionospheric  
303 disturbance information.



304

305

306

307

Figure 4 Normalized electron density spatio-temporal images

(A) Descending (daytime) electron density data spatio-temporal image; (B) Ascending (nighttime) electron density data spatio-temporal image; (C) The spatio-temporal range of the study area, same below.

308

## 4.2. Spatial and Temporal IPI Hotspots images before and after $M_w7.3$ Maduo earthquake

309

310

311

312

313

314

315

Seismological PI research indicates that the change window on different scales significantly affects the predictive efficacy of the PI method (Zhang *et al.*, 2017). To verify the effectiveness of the IPI method in extracting seismic ionospheric precursor information, we constructed models on various temporal scales and calculated to obtain IPI hotspot images for 90 days before and 7 days after the earthquake, as shown in Figures 5 and 6.

316

317

318

In Figures 5 and 6, the change windows (A) - (D) are set to 5, 10, 15, and 20 days respectively. The red pentagram marks the date of the Maduo earthquake. Based on this, we analyzed the IPI hotspot features of models constructed with different

319 change windows, as seen in Table 1.

320 Table 1 IPI hotspot features of models with different scale change windows

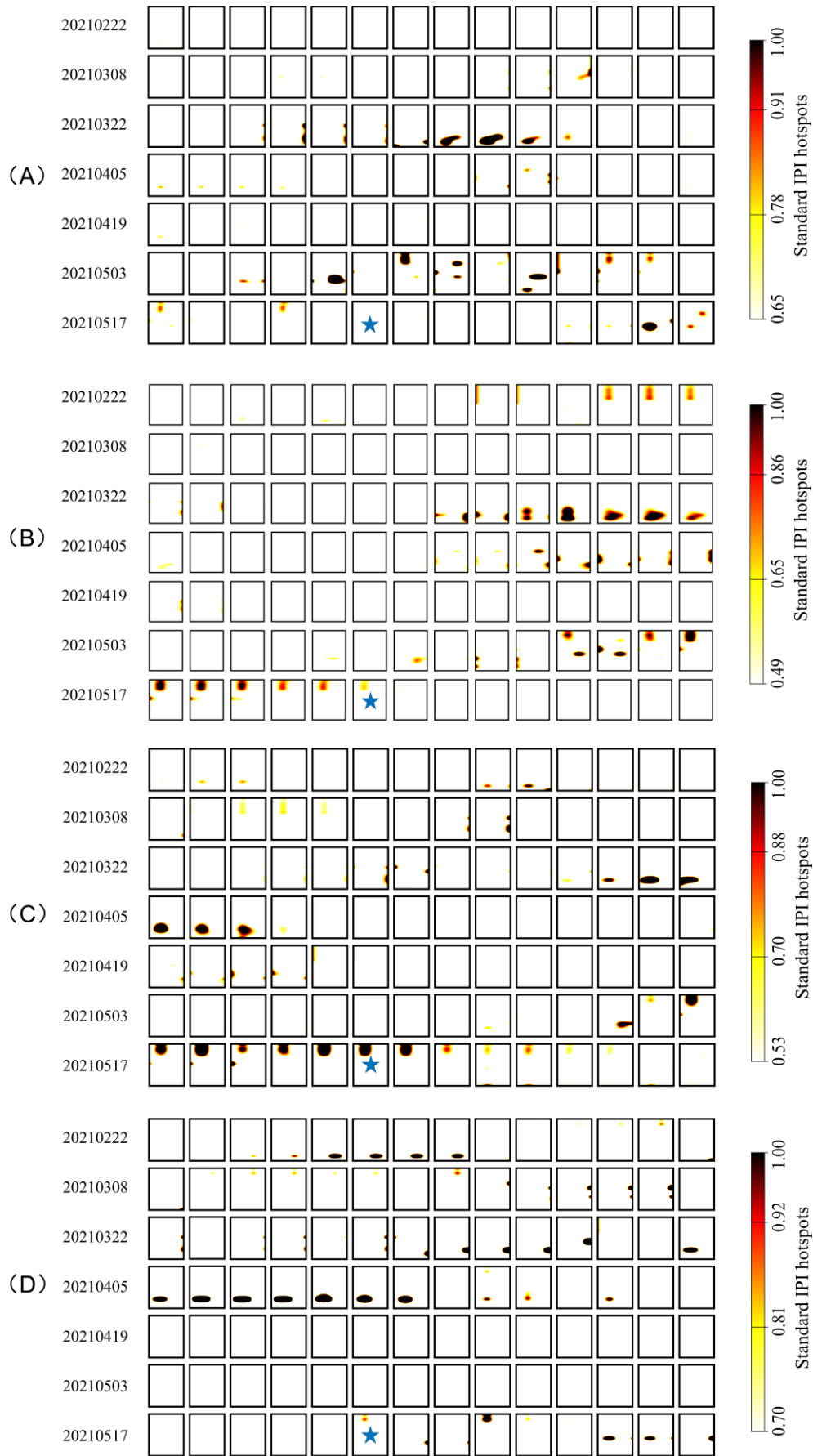
Change Window	5d	10d	15d	20d
IPI Hotspots features	IPI hotspots emerge before the earthquake, but their spatio-temporal distribution is disordered and chaotic	Continuous IPI hotspots appear before the earthquake and weaken before earthquake	Continuous IPI hotspots emerge before the earthquake and persist for a period after the earthquake	Continuous IPI hotspots appear after the earthquake

321 Based on the analysis of Figure 5, 6 and Table 1, We find:

322 (1) The IPI method can extract ionospheric anomalies from descending orbit  
 323 (daytime) data.

324 (2) Models constructed with different scale change windows can capture  
 325 ionospheric disturbances. However, there are differences in the disturbances detected  
 326 by each model. The IPI model with a change window of  $t_2-t_1=10$  days yields better  
 327 results in capturing anomalies before and after the earthquake.

328 (3) Models constructed with different scale change windows can capture  
 329 ionospheric disturbances. However, there are differences in the disturbances detected  
 330 by each model. The IPI model with a change window of  $t_2-t_1=10$  days yields better  
 331 results in capturing anomalies before and after the earthquake.

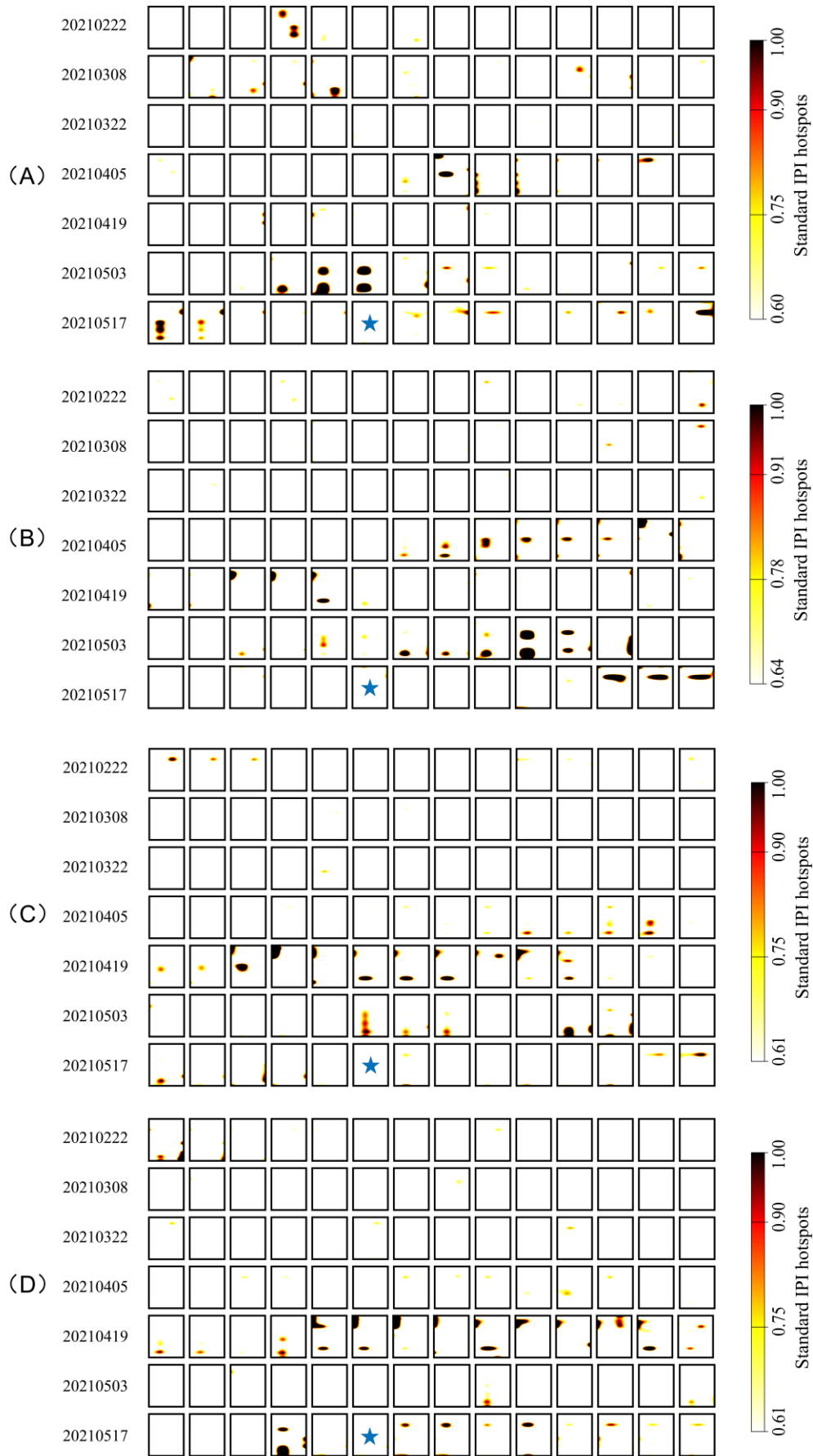


★ 20210522 Maduo  $M_w$  7.3 Earthquake

333  
334  
335

Figure 5 IPI hotspots image based on descending orbit data

(A)  $t_2-t_1=5d$ . (B)  $t_2-t_1=10d$ . (C)  $t_2-t_1=15d$ . (D)  $t_2-t_1=20d$ . The date on the left corresponds to the first image of each row, with the research area being the same as that in Figure 4.



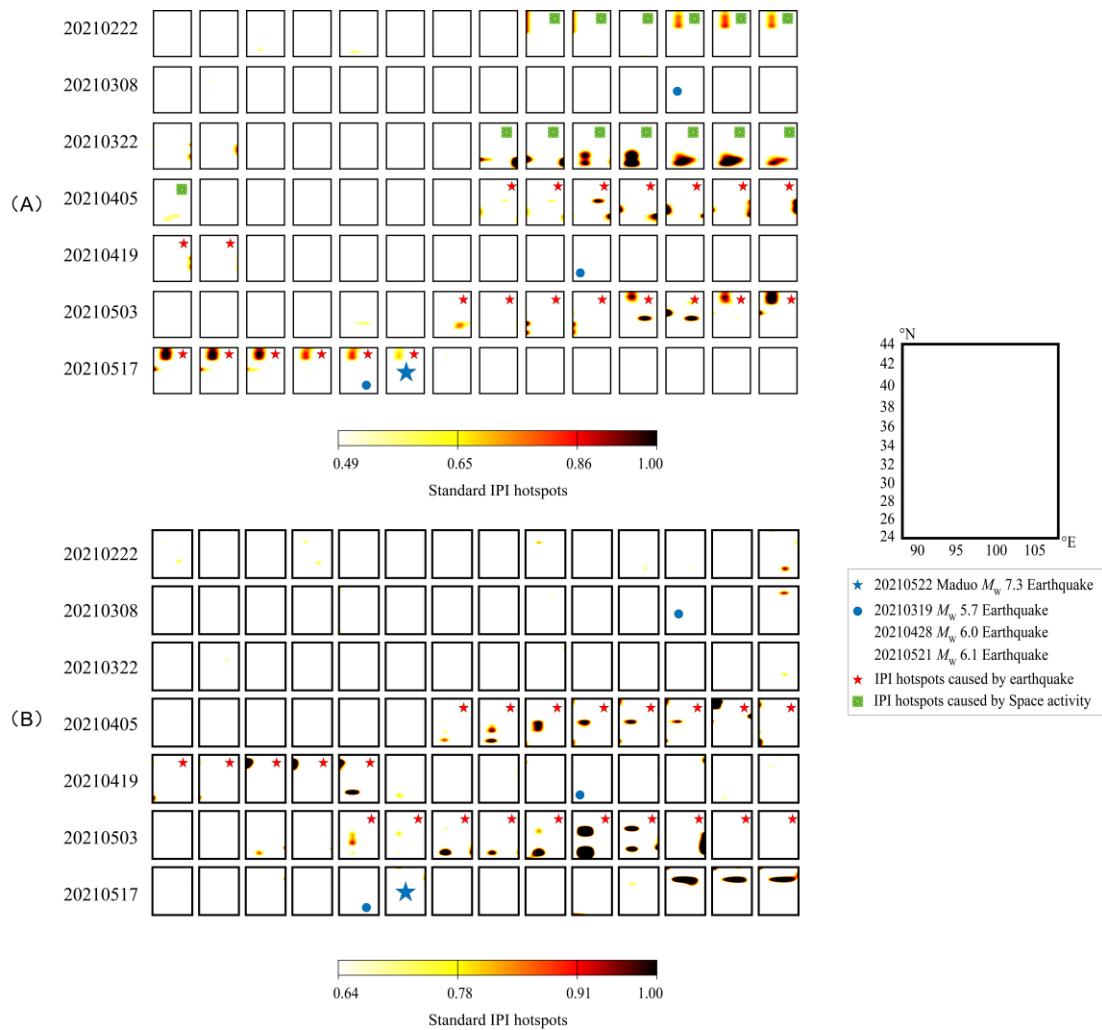
★ 20210522 Maduo  $M_w$  7.3 Earthquake

337 Figure 6 IPI hotspots image based on ascending orbit data  
338 (A)  $t_2-t_1=5d$ . (B)  $t_2-t_1=10d$ . (C)  $t_2-t_1=15d$ . (D)  $t_2-t_1=20d$ . The date on the left corresponds to the first image of  
339 each row, with the research area being the same as that in Figure 4.

## 340 5. Discussion

341 Based on the spatio-temporal evolution characteristics of CSES electromagnetic  
342 satellite observation data and earthquake-ionospheric precursor features, we optimize  
343 the PI method to develop the IPI method. Using the 2021 Maduo  $Mw7.3$  earthquake  
344 as a test case for the method's effectiveness and reliability, the results indicate that: 1)  
345 The IPI can extract ionospheric anomaly information from descending (daytime) data.  
346 2) Models constructed for different scale change windows can capture ionospheric  
347 disturbances, though the disturbances detected by each model differ, with the IPI  
348 model for a change window of  $t_2-t_1=10$  days obtaining better pre- and post-earthquake  
349 anomaly information. 3) The IPI hotspot maps calculated from descending (daytime)  
350 and ascending (nighttime) data show similarities in trends and differences in  
351 spatio-temporal locations.

352 The results of the Maduo  $Mw7.3$  earthquake demonstrate that the IPI method can  
353 extract significant ionospheric disturbance signals. Previous research has shown a  
354 significant statistical correlation between shallow earthquakes with magnitudes  
355  $M \geq 5.5$  and variations in the ionospheric anomalies (De Santis *et al.*, 2019, 2021; Yan  
356 *et al.*, 2017). The ionosphere is also influenced by multiple factors, such as solar  
357 activity, geomagnetic storms, and geomagnetic activities (Du *et al.*, 2022), and it  
358 remains unknown whether the anomalies present in Figures 5 and 6 are caused by the  
359 Maduo  $Mw7.3$  earthquake. To comprehensively analyze factors related to IPI hotspots,  
360 we will utilize earthquakes within the study area with  $Mw \geq 5.5$ , the Kp index  
361 indicating geomagnetic activity strength, the Dst index reflecting the intensity of  
362 geomagnetic storms, and the F10.7 index denoting solar activity (collectively referred  
363 to as space weather indices) for the analysis of IPI model hotspots in a change  
364 window of  $t_2-t_1=10$  days (Fejer *et al.*, 1991; Liu *et al.*, 2022).



365

366

Figure 7 IPI hotspots image for  $t_2-t_1=10d$

367

(A)Results of descending (daytime) data. (B) Results of ascending (nighttime) data. The date on the left

368

corresponds to the first image in each row. The blue pentagram represents the epicenter of the Maduo  $M_w$ 7.3

369

earthquake, and the blue circles mark earthquakes within the study area with magnitudes  $\geq M_w$ 5.5. The IPI hotspot

370

periods are divided into: March 2-7 (Period 1), March 29-April 5 (Period 2), April 12-20 (Period 3), May 9-23

371

(Period 4), April 11-24 (Period 5), and May 5-14 (Period 6). The red pentagrams indicate that the IPI hotspots in

372

these periods are caused by earthquakes, and the green suns indicate that they are caused by space weather

373

activities.

374

Within the spatio-temporal scope of the IPI study, three earthquakes with

375

$M_w \geq 5.5$  occurred: the March 19, 2021 Naqu, Xizang  $M_w$ 5.7 earthquake in China

376

(31.925°N, 92.915°E), the April 28 Dhekiajuli  $M_w$ 6.0 earthquake in India(26.781°N,

377

92.457°E), and the May 21  $M_w$ 6.1 Yangbi, Yunnan earthquake in China(25.727°N,

378

100.008°E). Based on the general empirical laws proposed by Rikitake (1987) and the

379

seismogenic zone empirical formula by Dobrovolsky (1979), the anomalous periods

380

for  $M_w=5.5$  and  $M_w=6.1$  earthquakes occurred approximately 16 and 26 days before

381 the earthquakes, respectively, mainly within a 400 km range. We will analyze the  
382 earthquake-IPI hotspots based on the aforementioned conditions.

383 The IPI method uses Boolean functions and a threshold  $N_C$  to determine  
384 anomalies, calculating the relative changes between the change window ( $t_1-t_2$ ) and the  
385 background window ( $t_b-t_1$ ), with the resulting anomaly values assigned to  $t_2$ . This  
386 means that the anomaly value at  $t_2$  depends on the frequency of electron density  
387 disturbances above  $N_C$  during the change window. If activities such as solar,  
388 geomagnetic, and magnetic storms occur within the change window and cause  
389 electron density disturbances greater than the threshold  $N_C$ , they will affect the IPI  
390 results, but the extent of the impact depends on the duration of these activities, i.e., the  
391 frequency of anomalies. Previous studies indicate that a Kp index over 3 suggests  
392 high geomagnetic activity, a Dst index greater than -30nT signals a geomagnetic  
393 storm, and an F10.7 index above 100 denotes solar activity (Li *et al.*, 2022).  
394 Assuming that these geomagnetic and solar activities cause disturbances in electron  
395 density, which exceed the threshold  $N_C$  only on the same day. We established that  
396 only when more than 50% of the change interval exhibits the aforementioned  
397 activities is an IPI hotspot attributed to geomagnetic, solar, or storm activities, termed  
398  $W_{IPI}$ . Hence, we computed the space weather indices for the entire study duration of  
399 the Maduo  $M_w7.3$  earthquake to locate intervals likely to produce  $W_{IPI}$ , as depicted in  
400 Figure 8.

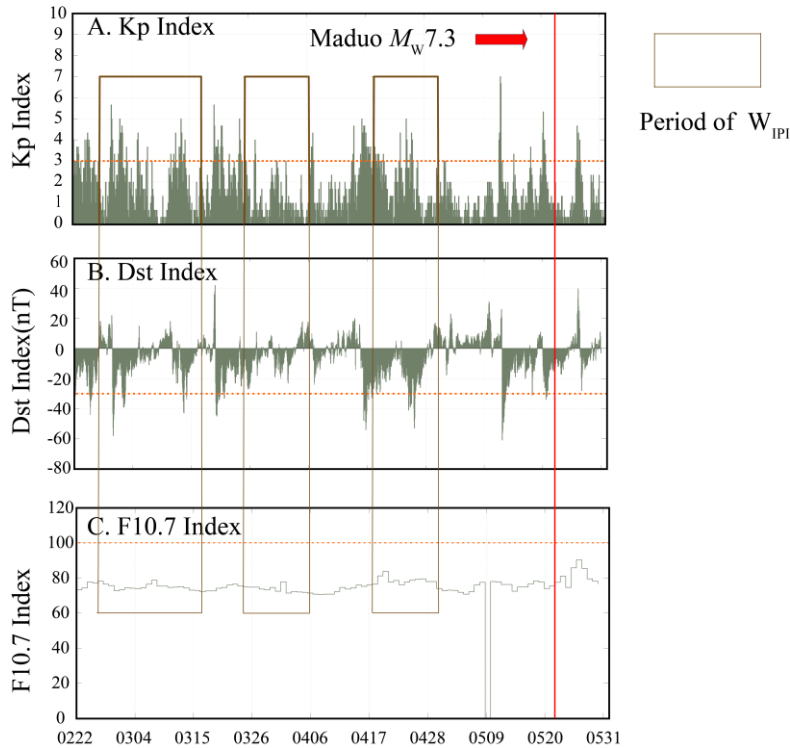


Figure 8 Space weather index image

(A) a bar chart of the Kp index. (B) a bar chart of the Dst index. (C) a step chart of the F10.7 index. Each index's threshold marked by an orange dashed line, and periods meeting the WIPI criteria highlighted with brown rectangles

According to the results in Figure 7 (A), the main IPI hotspots were concentrated in four periods in 2021: March 2-7 (Period 1), March 29 to April 5 (Period 2), April 12-20 (Period 3), and May 9-23 (Period 4). Figure 7 (B) shows that IPI hotspots were primarily distributed during two periods in 2021: April 11-24 (Period 5) and May 5-14 (Period 6). Based on the space weather index data in Figure 8, we calculated the primary periods for  $W_{IPI}$  to be February 27-28, March 1-17, March 26 - April 6, and April 19-30, 2021.

We analyzed the reasons for the IPI hotspot anomalies in each period, considering the intervals of  $W_{IPI}$  caused by space weather index anomalies and the spatial-temporal locations of earthquakes with  $M_w \geq 5.5$ . Before the emergence of hotspots in the northern part of the study area from March 2-7, 2021 (Period 1) and the southwestern part from March 29-April 5, 2021 (Period 2) in Figure 7 (A), there were multiple occurrences of geomagnetic activity and storms. The periods of February 27-28, March 1-17, and March 26-April 6, 2021, were identified as the main intervals for  $W_{IPI}$ , suggesting that the aforementioned hotspots might be related to

421 geomagnetic activities, among others. The hotspots in the eastern and western parts of  
422 the study area from April 12-20 (Period 3) and above and southwest of the epicenter  
423 from April 11-24 (Period 5) in Figure 7 (A) and (b) appeared before the  $W_{IPI}$  (April  
424 19-30). Although there is some overlap between Periods 3 and 5 and this  $W_{IPI}$ , the  
425 primary time frames of Periods 3 and 5 precede the  $W_{IPI}$ . Moreover, after the  
426 occurrence of this  $W_{IPI}$ , the spatio-temporal trends of the hotspots in Periods 3 and 5  
427 remained unchanged, unaffected by space weather. This indicates that the IPI hotspots  
428 during these periods are not related to solar activities, geomagnetic disturbances, or  
429 magnetic storms. They are likely related to crustal activities during the gestation of  
430 the April 28, 2021,  $Mw6.0$  earthquake and the Qinghai Maduo  $Mw7.3$  earthquake.  
431 Similarly, in Figure 7 (A), for May 9-23, 2021 (Period 4), the central and northern  
432 hotspots, and in Figure 7 (B), for May 5-14, 2021 (Period 6), the western and  
433 southwestern hotspots showed no significant geomagnetic storms or activity before  
434 their formation. Within 26 days following the anomalies, Yangbi  $Mw6.1$  and Maduo  
435  $Mw7.3$  earthquake occurred within 400 km of the IPI hotspots, suggesting a possible  
436 connection with the seismic preparation phase of these earthquakes. Others' research  
437 on ionospheric anomalies associated with the Maduo earthquake revealed that  
438 anomalies were detected in the Dobrovolsky seismogenic zone as early as April 10,  
439 2021, with intensification beginning about 20 days before the earthquake (Du *et al.*,  
440 2022) and significant increases in electron density observed approximately 14 days  
441 prior (Dong *et al.*, 2022; Li *et al.*, 2022).

442 We also observed that the evolution of IPI hotspots prior to the Maduo  
443 earthquake follows a pattern of appearance, persistence, disappearance, re-appearance,  
444 and re-disappearance. Previous models of lithospheric coupling, involving radon gas  
445 release due to rock layer activity, earth degassing caused by fluid migration, and the  
446 release of p-holes (positive holes), suggest that this trend is likely due to  
447 physicochemical changes in the lithosphere during the earthquake's gestation process  
448 (Hayakawa *et al.*, 2004; Pulinets *et al.*, 2011; Parrot *et al.*, 2021). Similar ionospheric  
449 anomaly processes have also been observed in multi-layered coupling studies of the  
450 2013 Lushan  $Mw6.7$  earthquake and the 2018 Indonesian  $Mw7.5$  earthquake  
451 (Marchetti *et al.*, 2020; Zhang *et al.*, 2022). Statistical studies based on SWARM

452 satellite electron density and magnetic field data revealed that anomalies before  
453  $M_w \geq 5.5$  earthquakes are not limited to a specific time frame but occur in multiple  
454 intervals. This supports the theory that the recurring anomalies detected in our IPI  
455 hotspots might result from multi-layered coupling during the earthquake preparation  
456 phase. However, there is currently no mature theoretical model or mechanism for how  
457 earthquakes affect the ionosphere. The reasons why IPI hotspots exhibit such  
458 distinctive earthquake-ionosphere disturbance signals remain to be further explored in  
459 multi-layered coupling research.

460 IPI hotspots shows anomalies from around 40 days to approximately 15 days  
461 before earthquakes, extracting their spatio-temporal evolution process. This  
462 demonstrates the feasibility and effectiveness of this method in extracting seismic  
463 ionospheric anomaly data. This primarily relies on the adaptive nature of the IPI  
464 algorithm, which can mitigate the effects of background changes and noise to a  
465 certain extent. While the IPI method can capture the continuous spatio-temporal  
466 changes in ionospheric parameter anomalies, it still has many limitations in practical  
467 earthquake forecasting:

468 1) The space environment is influenced by various factors. The IPI method can  
469 only extract anomalies in ionospheric parameters but cannot directly filter out  
470 ionospheric precursor information caused by earthquakes. It is challenging to  
471 determine which earthquake caused the ionospheric anomalies in regions with  
472 multiple significant earthquakes. Establishing anomaly determination indicators and  
473 combining them with space weather indices like Kp and Dst for anomaly filtering  
474 could be an effective solution.

475 2) We use R from Dobrovolsky empirical formula,  $R = 10^{0.43M}$ , as the radius of  
476 the circumscribed circle of the rectangular study area to ensure it falls within the  
477 seismogenic zone. However, considering that magnetic field lines are not  
478 perpendicular to the ground and phenomena such as  $E \times B$  drift and plasma diffusion  
479 occur during signal propagation (Liu *et al.*, 2021), it is possible for earthquake  
480 ionospheric anomalies to appear outside the seismogenic zone. This understanding,  
481 also noted by Marchetti *et al.* (2020). Suggests that future research areas might need  
482 to be adjusted accordingly.

483 3) The study separately utilized descending (daytime) and ascending (nighttime)  
484 orbit data and designed periods of change window across different time scales for  
485 method testing. Although different IP models were able to extract distinct ionospheric  
486 anomaly disturbance signals, there were differences in the spatio-temporal distribution  
487 of these anomalies. This indicates that data selection and parameter setting greatly  
488 influence the final results of the IPI method. The setting of optimal parameters and the  
489 selection of data require further research.

## 490 **6. Conclusion**

491 Based on the PI method, we optimized the data processing by combining features  
492 of satellite observations and earthquake-ionospheric precursor characteristics, leading  
493 to the establishment of the IPI method. The method's reliability and effectiveness were  
494 validated using the 2021 *Mw*7.3 Maduo earthquake in Qinghai, China, as a case study.  
495 The IPI calculation provided continuous spatio-temporal images of electron density  
496 anomalies, and potential earthquake-ionosphere anomaly disturbance signals were  
497 analyzed based on space weather indices and IPI hotspots.

498 The main research findings are as follows:

499 1) Based on CSES electron density data, the model constructed by the IPI  
500 method was able to extract electron density anomaly disturbance signals not  
501 presenting in normalized electron density spatio-temporal images, in both descending  
502 (daytime) and ascending (nighttime) orbits, and across various scales of change  
503 window.

504 2) Anomalies in electron density appeared about 40 days before the Maduo  
505 *Mw*7.3 earthquake, exhibiting an evolution process of  
506 “appearance-continuation-disappearance-reappearance-disappearance”. The IPI  
507 hotspot maps derived from descending (daytime) and ascending (nighttime) data  
508 showed similar trends.

509 The IPI method, with its high spatio-temporal resolution and adaptability to  
510 remove background trends and noise, can capture the spatio-temporal evolution of  
511 ionospheric parameters over and around earthquake areas, as well as potential strong  
512 seismic ionospheric anomaly signals. Such capabilities are instrumental in  
513 investigating the physical mechanisms behind the earthquake-ionosphere coupling

514 process. However, accurately identifying earthquake ionospheric precursors from  
515 electromagnetic satellite data remains a challenging task. Due to the complexity of  
516 earthquake preparation mechanisms, the discontinuity of observational data, and  
517 limitations in data analysis methods, numerous challenges persist, requiring a  
518 multidisciplinary approach to address them. Finally, it is important to acknowledge  
519 that the research on the IPI method is in its early stages, necessitating ongoing  
520 optimization of the method and statistical analysis of seismic instances.

## 521 **Acknowledgement**

522 We are grateful to Prof. Chen Chien-Chih of National Central University at  
523 Taiwan for providing the PI code, and to Prof. Wu Zhongliang, Zhang Xuemin, Liu  
524 Jing, and master's student Dong Lei of the Institute of Earthquake Prediction, China  
525 Earthquake Administration (IEPCA), for their help in constructing the idea of the  
526 thesis, data processing. CSES satellite data were obtained from (<http://leos.ac.cn>),  
527 F10.7 index and Kp index data were obtained from the German Center for  
528 Geoscientific Research (<https://www.gfz-potsdam.de/>), Dst index was obtained from  
529 the Geomagnetic Data Center of Kyoto University at Japan  
530 (<https://wdc.kugi.kyoto-u.ac.jp/wdc/Sec3.html>), and seismic catalogs were obtained  
531 from USGS (<https://wdc.kugi.kyoto-u.ac.jp/wdc/Sec3.html>). This work was funded by  
532 the National Key Research and Development Program of the Ministry of Science and  
533 Technology of China (2018YFE0109700), the National Natural Science Foundation  
534 of China(60214402) and the Joint Fund for Earthquake of the National Natural  
535 Science Foundation of China (U2039207). All figures were drawn using GMT  
536 (Wessel *et al.*, 2019).

## 537 **References**

- 538 1.Chang X, Zou B, Guo J, et al. 2017. One sliding PCA method to detect ionospheric  
539 anomalies before strong Earthquakes: Cases study of Qinghai, Honshu, Hotan  
540 and Nepal earthquakes. *Advances in Space Research*, 59: 2058-2070.
- 541 2.Chen C, Rundle J, Holliday J, et al. 2005. The 1999 Chi-Chi, Taiwan, earthquake as  
542 a typical example of seismic activation and quiescence. *Geophysical Research*  
543 *Letters*, 32(22): L22315.
- 544 3.Dobrovolsky I, Zubkov S, Miachkin V. 1979. Estimation of the size of earthquake  
545 preparation zones. *Pure and Applied Geophysics*, 117: 1025-1044.

- 546 4.Dong L, Zhang X, Du X. 2022. Analysis of Ionospheric Perturbations Possibly  
547 Related to Yangbi Ms6.4 and Maduo Ms7.4 Earthquakes on 21 May 2021 in  
548 China Using GPS TEC and GIM TEC Data. *Atmosphere*, 13: 1725.
- 549 5.Du X, Zhang X. 2022. Ionospheric Disturbances Possibly Associated with Yangbi  
550 Ms6.4 and Maduo Ms7.4 Earthquakes in China from China Seismo  
551 Electromagnetic Satellite. *Atmosphere*, 13: 438.
- 552 6.Fejer B, Paula E, Gonzales S, et al. 1991. Average vertical and zonal F-region  
553 plasma drifts over Jicamarca. *Journal of Geophysical Research Atmospheres*, 96:  
554 13901-13906.
- 555 7.Gokhberg M B, Morgounov V A, Yoshino T, et al. 1982. Experimental measurement  
556 of electromagnetic emissions possibly related to earthquakes in Japan. *J.*  
557 *Geophys. Res*, 87: 7824-7828.
- 558 8.Guo Y, Zhang X, Liu J, et al. 2022. Seismo-Ionospheric Effects Prior to Two  
559 Earthquakes in Taiwan Detected by the China Seismo-Electromagnetic  
560 Satellite. *Atmosphere*, 13(9): 1523.
- 561 9.Hayakawa M, Molchanov O A, Team N, et al. 2004. Summary report of NASDA's  
562 earthquake remote sensing frontier project. *Phys. Chem. Earth*, 29: 617–625.
- 563 10.Li M, Jiang X, Li J, et al. 2023. Temporal-spatial characteristics of  
564 Seismo-ionospheric influence observed by the CSES satellite. *Advances in Space*  
565 *Research*, doi: <https://doi.org/10.1016/j.asr.2023.07.044>.
- 566 11.Li M, Shen X, Parrot, M, et al. 2020. Primary joint statistical seismic influence on  
567 ionospheric parameters recorded by the CSES and DEMETER satellites, *Journal*  
568 *of Geophysical Research: Space Physics*, 125, e2020JA028116.
- 569 12.Li M, Wang H, Liu J, et al. 2022. Two Large Earthquakes Registered by the CSES  
570 Satellite during Its Earthquake Prediction Practice in China. *Atmosphere*, 13:  
571 751.
- 572 13.Liu J, Zhang X, Yang X, et al. 2023. The Analysis of Lithosphere–Atmosphere–  
573 Ionosphere Coupling Associated with the 2022 Luding Ms6.8 Earthquake.  
574 *Remote Sens*. 15: 4042.
- 575 14.Liu J, Guan Y, Zhang X, et al. 2021. The data comparison of electron density  
576 between CSES and DEMETER satellite, Swarm constellation and IRI model.  
577 *Earth and Space Science*, 8, e2020EA001475.
- 578 15.Liu J, Qiao X, Zhang X, et al. 2022. Using a Spatial Analysis Method to Study the  
579 Seismo-Ionospheric Disturbances of Electron Density Observed by China  
580 Seismo-Electromagnetic Satellite. *Front. Earth Sci*, 10: 811658.
- 581 16.Li X, Xu Y, An Z, et al. 2019. The high-energy particle package onboard CSES.  
582 *Radiation Detection Technology and Methods*, 3(3): 11.
- 583 17.Li Z, Yang B, Huang J, et al. 2022. Overview of space-based electric field data

- 584 processing methods. *Progress in Geophysics*, 1-15(In Chinese).
- 585 18.Marchetti D, Santis D, Shen X, et al. 2019. Possible  
586 Lithosphere-Atmosphere-Ionosphere Coupling effects prior to the 2018  $M_w=7.5$   
587 Indonesia earthquake from seism, atmospheric and ionospheric data. *Journal of*  
588 *Asian Earth Sciences*, 188: 104097.
- 589 19.Parrot M, Tramutoli V, Liu T, et al. 2021. Atmospheric and ionospheric coupling  
590 phenomena associated with large earthquakes. *Eur. Phys. J. Spec. Top*, 230: 197–  
591 225 2021.
- 592 20.Pulinets S, Ouzounov D. 2011. Lithosphere-Atmosphere-Ionosphere Coupling  
593 ( LAIC ) model: An unified concept for earthquake precursors validation.  
594 *Journal of Asian Earth Sciences*, 41(4/5): 371-382.
- 595 21.Rikitake T. 1987. Earthquake precursors in Japan: precursor time and detectability.  
596 *Tectonophysics*,136: 265–282.
- 597 22.Rundle J, Klein W, Tiampo K, et al. 2000. Linear pattern dynamics in nonlinear  
598 threshold systems. *Physical Review E*, 61(3): 2418.
- 599 23.Rundle J, Tiampo K, Klein W, et al. 2002. Self-organization in leaky threshold  
600 systems: The influence of near-mean field dynamics and its implications for  
601 earthquakes, neurobiology, and forecasting. *Proceedings of the National*  
602 *Academy of Sciences*, 99(suppl 1): 2514-2521.
- 603 Santis D, Marchetti D, Pavón-Carrasco F, et al. 2019. Precursory worldwide  
604 signatures of earthquake occurrences on Swarm satellite data. *Sci Rep*, 9: 20287.
- 605 24.Santis D, Marchetti D, Perrone L, et al. 2021. Statistical Correlation Analysis of  
606 Strong Earthquakes and Ionospheric Electron Density Anomalies as Observed by  
607 CSES-01. *Il Nuovo Cimento C*, 44: 1–4.
- 608 25.Shen X, Yuan S, Zhima Z. 2023. Expanding Global Geophysical Field and Space  
609 Environment Sensing Modeling Capabilities - The 5th Anniversary of ZH-1  
610 Satellite in Orbit. *Space International*, 03: 31-37 ( in Chinese ) .
- 611 26.Shen X, Zhang X, Yuan S, et al. 2018. The state-of-the-art of the China  
612 Seismo-Electromagnetic Satellite mission. *Sci China Tech Sci*, 61: 634–642
- 613 27.SONDHIYA D, KUMAR S, GWAL A. 2014. On the possibility of precursors of  
614 earthquakes in VLF range observed by DEMETER Satellite. *Nonlinear*  
615 *Processes in Geophysics Discussions*, 1: 977-997.
- 616 28.Spogli L, Sabbagh D, Regi M, et al. 2021. Ionospheric response over Brazil to the  
617 August 2018 geomagnetic storm as probed by CSES-01 and Swarm satellites and  
618 by local ground-based observations, *Journal of Geophysical Research: Space*  
619 *Physics*, 126, e2020JA028368.

- 620 29. Tiampo K, Rundle J, McGinnis S, et al. 2002. Eigenpatterns in southern California  
621 seismicity, *J. Geophys. Res*, 107(B12): 2354.
- 622 30. Wessel P, Luis J, Uieda L, et al. 2019. The Generic Mapping Tools version  
623 6. *Geochemistry, Geophysics, Geosystems*, 20: 5556–5564.
- 624 31. Wu A, Zhang Y, Zhou Y, et al. 2011. On the spatial-temporal characteristics of  
625 ionospheric parameters before Wenchuan earthquake with the MPI method.  
626 *Chinese Journal of Geophysics*, 54(10): 2445-2457(in Chinese).
- 627 32. Yan R, Parrot M, Pinçon J. 2017. Statistical study on variations of the ionospheric  
628 ion density observed by DEMETER and related to seismic activities. *J. Geophys.*  
629 *Res. Space Phys*, 122.
- 630 33. Yan R, Zhima Z, Xiong C, et al. 2020. Comparison of electron density and  
631 temperature from the CSES satellite with other space-borne and ground-based  
632 observations. *J. Geophys. Res. Space Phys*, 125, e2019JA027747.
- 633 34. Yao L, Zhang X, Yu T. 2014. A study of spacial correlation of monthly mean  
634 deviation of ionospheric TEC over China. *Chinese Journal of Geophysics*, 57(11):  
635 3600-3610 (in Chinese).
- 636 35. Yang C, Yong S, Wang X, et al. 2021. Research on Indonesia Ms7.4 Earthquake  
637 Based on Data of Zhangheng-1 Electromagnetic Satellite. *Acta Scientiarum*  
638 *Naturalium Universitatis Pekinensis*, 57(06): 997-1005.
- 639 36. Yang Y, Hulot G, Vigneron P, et al. 2021. The CSES global geomagnetic field  
640 model (CGGM): an IGRF-type global geomagnetic field model based on data  
641 from the China Seismo-Electromagnetic Satellite, *Earth Planets Space*. 73: 45.
- 642 37. Zhang S, Zheng J, Jiang C, et al. 2017. Optimal analysis of parameter settings in  
643 pattern informatics(PI) algorithm: An example of Shandong and adjacent areas.  
644 *Chinese Journal of Geophysics*, 60(12): 4633-4643 (in Chinese).
- 645 38. Zhang X, Wang Y, Boudjada MY, et al. 2020 Multi-Experiment Observations of  
646 Ionospheric Disturbances as Precursory Effects of the Indonesian Ms6.9  
647 Earthquake on August 05, 2018. *Remote Sensing*, 12(24): 4050.
- 648 39. Zhang Y, Li M, Huang Q, Shao Z, et al. 2023. Statistical correlation between  
649 DEMETER satellite electronic perturbations and global earthquakes with  $M \geq 4.8$ .  
650 *IEEE TRANSACTIONS ON GEOSCIENCE AND REMOTE SENSING*, 61: 1-18.
- 651 40. Zhang Y, Wang T, Chen W, et al. 2023. Are There One or More Geophysical  
652 Coupling Mechanisms before Earthquakes? The Case Study of Lushan (China)  
653 2013. *Remote Sensing*, 15: 1521.
- 654 41. Zhao S, Shen X, Li L, et al. 2021. A lithosphere-atmosphere-ionosphere coupling  
655 model for ELF electromagnetic waves radiated from seismic sources and its  
656 possibility observed by the CSES. *Science China(Technological Sciences)*, 64  
657 (11): 2551-2559.

- 658 42.Zheng L, Yan R, Parrot M, et al. 2022. Statistical Research on Seismo-Ionospheric  
659 Ion Density Enhancements Observed via DEMETER. *Atmosphere*, 13: 1252.
- 660 43.Zhuo X, Zhao G, Wang J, et al. 2005. Seismo-Electromagnetic Satellite in  
661 Earthquake Prediction. *Journal of Geodesy and Geodynamics*, 02: 1-5.